

Down-bending Breaks in Galactic Disks Are an Intrinsic Byproduct of Inside-out Growth

LIUFEI CHEN (陈柳霏),^{1,2} MIN DU (杜敏),² SHUAI LU (卢帅),² JING LI (李静),¹ AND LUIS C. HO^{3,4}

¹*School of Physics and Astronomy, China West Normal University, 1 ShiDa Road, Nanchong 637002, China*

²*Department of Astronomy, Xiamen University, Xiamen, Fujian 361005, China*

³*Kavli Institute for Astronomy and Astrophysics, Peking University, Beijing 100871, China*

⁴*Department of Astronomy, School of Physics, Peking University, Beijing 100871, China*

ABSTRACT

The exponential profile has long been hypothesized as the fundamental morphology of galactic disks. The IllustrisTNG simulations successfully reproduce diverse surface-density profiles: Type I (single exponential), Type II (down-bending), and Type III (up-bending), matching reasonably well with observed mass-size relations and kinematics. Type II disks dominate the stellar mass regime $M_\star < 10^{10.6} M_\odot$ with a prevalence of $\sim 40\%$, exhibiting systematically extended morphologies. Conversely, Type III and Type I galaxies occupy more compact configurations, following the same mass-size scaling relation. Evolutionary history analysis shows that Type II galaxies experience minimal external perturbation, representing the intrinsic disk form—challenging conventional single-exponential paradigms. We demonstrate that Type II breaks arise naturally via inside-out growth during $z < 1$, governed by synchronized cold-gas accretion and localized specific star formation rate peaks. This mechanism also produces the characteristic U-shaped age profiles of Type II disks. Crucially, dynamical redistribution of stars plays an unimportant role in their formation.

Keywords: Galaxies (573) — Galaxy kinematics (602) — Galaxy formation (595) — Galaxy structure (622) — Galaxy stellar disks (1594) — Astronomy simulations (1857)

1. INTRODUCTION

It has long been recognized that galactic disk radial surface-brightness profiles are described by an exponential function (K. C. Freeman 1970). However, deviations are frequently observed in the outer regions, which are typically classified into three distinct categories: Type I (single-exponential), Type II (down-bending), and Type III (up-bending) (P. Erwin et al. 2005; M. Pohlen & I. Trujillo 2006). Single-exponential (Type I) disks are widely regarded as the natural baseline configuration in theoretical models (e.g., H. Mo et al. 1998; F. C. Van Den Bosch 2001; A. A. Dutton & F. C. Van Den Bosch 2009) as well as morphological decomposition in observations (e.g., C. Y. Peng et al. 2010; S. Díaz-García et al. 2016). E. Wang & S. J. Lilly (2022) suggested that the exponential profile of disk galaxies can be a natural product due to the viscosity of gas.

The distribution of these disk profiles exhibits a dependence on stellar mass, Hubble type, and local en-

vironment. Type II profiles are prevalent in the mass range $\log(M_\star/M_\odot) \approx 9.5\text{--}10.5$, whereas Type III profiles dominate the high-mass regime, $\log(M_\star/M_\odot) \gtrsim 10.5$ (Y. Tang et al. 2020). This mass dependence is reflected in morphology: Type II profiles occur more frequently in late-type, disk-dominated galaxies, while Type III profiles are more characteristic of early-type systems (M. Pohlen & I. Trujillo 2006; L. Gutiérrez et al. 2011; J. Laine et al. 2016; Y. Tang et al. 2020). The Milky Way has also been found to follow a Type II break profile (H.-F. Wang et al. 2018; J. Lian et al. 2024, 2025). U-shaped average age profiles have been found to be prevalent in Type II disk galaxies (R. S. De Jong et al. 2007; D. J. Radburn-Smith et al. 2012; D. A. Dale et al. 2015), although T. Ruiz-Lara et al. (2015) argued that the U-shaped age profiles and Type II breaks are not necessarily coupled. Moreover, the characteristic Type II break radius scales positively with galaxy mass and has been observed to shift outward over cosmic time (I. Trujillo & M. Pohlen 2005; R. Azzollini et al. 2008; M. Pohlen & I. Trujillo 2006).

Various physical processes have been invoked to explain the formation of Type III profiles, involving ei-

ther internal dynamical evolution or external environmental effects. Internally, galactic bars can scatter stars from circular orbits onto large, elongated trajectories (M. Brunetti et al. 2011), effectively transforming Type I or II profiles into Type III configurations (J. Herpich et al. 2017; T. Ruiz-Lara et al. 2017). Externally, minor mergers and tidal interactions redistribute stellar material via tidal torques that propel inner stars outward (J. D. Younger et al. 2007). Additionally, stellar material stripped from satellite galaxies during mergers adds directly to the light of the outer regions (A. P. Cooper et al. 2013).

The formation mechanisms of Type II breaks also remain a subject of active debate, primarily centered on two proposed scenarios. The first attributes Type II formation to radial migration and resonance-driven redistribution, where non-axisymmetric features, such as bars and spiral arms, are able to transport stars from the inner disk to beyond the break radius (V. P. Debattista et al. 2006; J. Herpich et al. 2017). While this framework can explain observed U-shaped age profiles (Z. Zheng et al. 2015; D. A. Dale et al. 2015), recent work suggests that such redistribution may eventually smooth out or erase these breaks (P. Sánchez-Blázquez et al. 2009; Y. Tang et al. 2020). The second scenario involves an abrupt change in the radial star formation profile. Simulation studies indicate that Type II disks may predominantly emerge from truncated star-forming disks (J. L. Pfeffer et al. 2022). Observationally, these galaxies exhibit down-bending radial star formation rate (SFR) profiles (Y. Tang et al. 2020). However, while this may explain the observed radial truncation, it struggles to account for the old stellar populations at large radii; these may generally require supplementary radial migration (R. Roškar et al. 2008; Y. Tang et al. 2020) or an extended stellar halo (J. L. Pfeffer et al. 2022).

The occurrence of Type II profiles may also be influenced by environment, with a notable suppression observed in cluster galaxies (P. Erwin et al. 2012; M. Mondelin et al. 2025b). J. L. Pfeffer et al. (2022) linked this reduced Type II fraction to the generally lower star-formation rates in cluster environments, suggesting that Type II disks may fade into Type I profiles once star formation ceases. This view is supported by P. Sánchez-Alarcón et al. (2023), who found a higher fraction of perturbations in field Type II disk galaxies ($42\% \pm 19\%$) compared to Type I ($17\% \pm 17\%$), implying that perturbations may drive Type II formation by enhancing star formation. Conversely, M. Mondelin et al. (2025a) propose that Type II profiles originate from internal processes such as disk instabilities and resonances during early formation phases, and are subsequently eroded by

the cluster environment. These conflicting perspectives highlight a key uncertainty: whether the Type II profile is a transient feature associated with star formation or instead arises from internal disk evolution. The latter scenario would potentially challenge the traditional view of the Type I profile as the fundamental baseline.

In this study, we analyze central disk galaxies (stellar mass $M_\star > 10^{10} M_\odot$) from the IllustrisTNG hydro-cosmological simulations, classifying systems into Types I, II, and III through fits to their stellar mass surface density profiles. This approach directly addresses the origin of observed disk morphological diversity. We subsequently focus on deciphering Type II break formation mechanisms and their signature U-shaped stellar age profiles. A new channel for forming Type II break is proposed. The paper is structured as follows: Section 2 details the simulation data, galaxy selection criteria, and profile extraction methodology; Section 3 presents statistical properties and comparative analysis of all three disk types; Section 4 investigates the physical drivers of Type II breaks and associated star-formation trends; Section 5 synthesizes implications and summarizes key conclusions.

2. METHODOLOGY: SAMPLE SELECTION AND CLASSIFICATION

2.1. *The IllustrisTNG project*

The IllustrisTNG project (F. Marinacci et al. 2018; J. P. Naiman et al. 2018; D. Nelson et al. 2018a, 2019a; A. Pillepich et al. 2018, 2019; V. Springel et al. 2018) is a suite of cosmological magnetohydrodynamical simulations executed with the moving-mesh code AREPO (V. Springel 2010), performed within the standard Λ CDM cosmology adopting Planck Collaboration et al. (2016) parameters: $\Omega_m = 0.3089$, $\Omega_\Lambda = 0.6911$, $\Omega_b = 0.0486$, $h = 0.6774$, $\sigma_8 = 0.8159$, and $n_s = 0.9667$. The project includes three simulation runs (TNG300, TNG100, TNG50) with varying volumes and resolutions (A. Pillepich et al. 2018; D. Nelson et al. 2019b). Compared to the original Illustris simulation, TNG incorporates improved models for chemical enrichment, stellar and black hole feedback, and cosmic magnetism (R. Weinberger et al. 2017; A. Pillepich et al. 2018). We utilize TNG50-1 (hereafter TNG50), which provides the highest resolution for studying stellar structures in galaxy peripheries. TNG50 employs 2×2160^3 initial resolution elements within a ~ 50 comoving Mpc periodic volume, achieving baryon mass resolution of $8.41 \times 10^4 M_\odot$ and dark matter particle mass of $4.57 \times 10^5 M_\odot$. The gravitational softening length is 0.29 kpc for dark matter and stellar particles at $z = 0$, with minimum gas softening length of 0.074 comoving

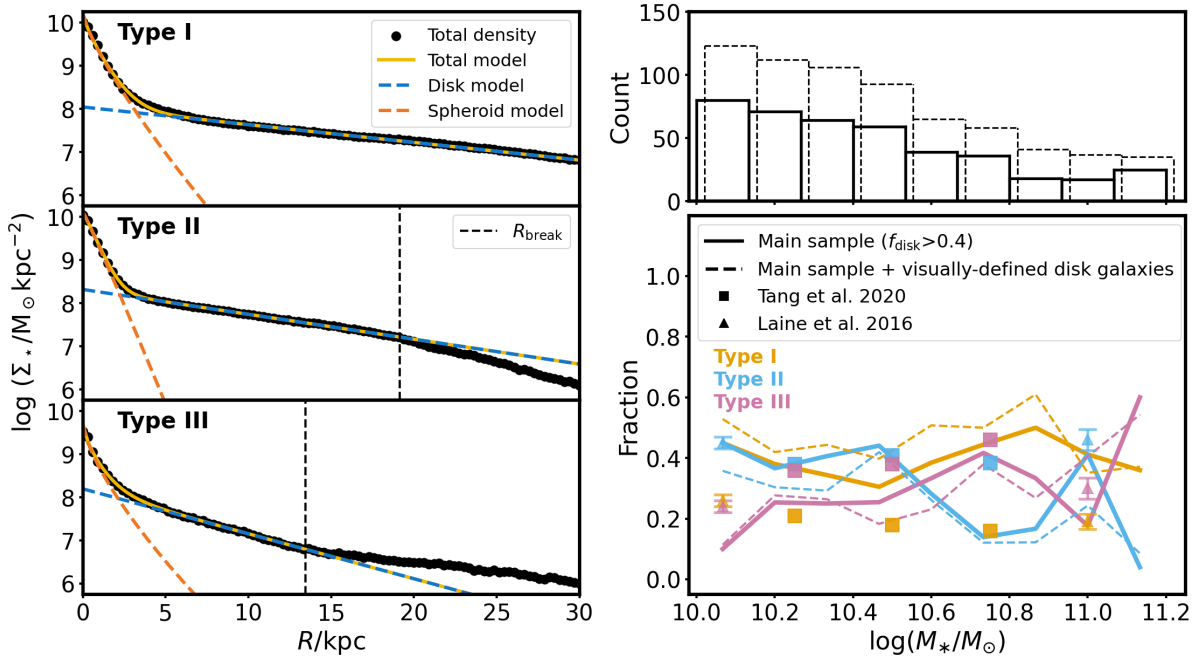


Figure 1. **Left panels:** Examples of surface density profiles (black dots) of galaxies with Type I, II, and III disks, from top to bottom. The exponential (blue-dashed lines) and Sérsic (orange-dashed) functions are used to decompose the disk and bulge component in morphology, their combined fitting results correspond to the yellow solid profiles. Vertical black dashed lines mark the break radius (R_{break}), where the profile first deviates from the inner exponential part. **Right panels:** The fraction of galaxies with different disk types as a function of their stellar masses. Solid and dashed lines denote results from two galaxy samples: our kinematically-selected primary sample ($f_{\text{disk}} > 0.4$; M. Du et al. (2019, 2020)) and a morphologically-defined sample incorporating visually classified disks to enable direct comparison with observational surveys (Y. Tang et al. 2020; J. Laine et al. 2016). The upper panel gives their number counts in each stellar mass bin.

kpc. These resolutions enable accurate reproduction of kinematic properties for galaxies with $M_* \geq 10^9 M_\odot$ (A. Pillepich et al. 2019).

We use friends-of-friends (FOF) (M. Davis et al. 1985) and SUBFIND (V. Springel et al. 2001) to identify halos and subhalos. Galaxies are defined as gravitationally bound particles within their host subhalos (stars, gas, dark matter, black holes). Each galaxy is oriented face-on based on stellar angular momentum and centered at the gravitational potential minimum, with bulk velocity subtracted.

2.2. Sample selection

We study disk galaxy profile types using a main sample of disk galaxies selected from the TNG50 simulation (A. Pillepich et al. 2019). Such a sample is selected via three criteria: inclusion of only central galaxies to minimize environmental effects; a stellar mass cutoff $M_* > 10^{10} M_\odot$, where M_* is computed from all stellar particles bound to the subhalo by SUBFIND, ensuring reliable kinematic property reproduction; and a disk mass fraction requirement $f_{\text{disk}} > 0.4$ within three half-mass effective radii to guarantee prominent disk structures. Our main sample meeting all criteria comprises

423 galaxies, with their stellar mass distribution shown as the solid-black histogram in Figure 1’s upper-right panel. The disk mass fraction f_{disk} is calculated via the dynamical decomposition method (see details in M. Du et al. 2019, 2020)¹, which employs automatic Gaussian Mixture Models (called auto-GMM) to cluster stellar particles in the kinematic phase space of circularity ($\varepsilon = j_z/j_c$, where j_z is the stellar angular momentum along the rotation axis and j_c is that of a circular orbit at the same binding energy), binding energy, and non-azimuthal angular momentum (M. G. Abadi et al. 2003; M. Doménech-Moral et al. 2012). Components with mean circularity $\langle j_z/j_c \rangle > 0.5$ are classified as disks: cold disks ($\langle j_z/j_c \rangle > 0.85$) and warm disks ($0.5 \leq \langle j_z/j_c \rangle \leq 0.85$). This technique isolates a kinematically distinct disk component from the composite spheroid (encompassing both bulges and halos). The resulting dynamics-based decomposition is fundamental for analyzing disk profiles, as it enables us to probe how disks and spheroids differentially shape profile types.

¹ The data of kinematic structures in TNG galaxies are publicly accessible at <https://www.tng-project.org/data/docs/specifications/#sec5m>

Our $f_{\text{disk}} > 0.4$ threshold aligns with kinematically-defined disk galaxies and fast rotators, as suggested by [W. Zhong et al. \(2026\)](#). Such a criterion corresponds approximately to a cylindrical rotation energy significance of $\kappa_{\text{rot}} > 0.5$ ([L. V. Sales et al. 2010](#))—a widely-used criterion for identifying simulated disk galaxies.

To enable robust comparison with observations, we supplement our analysis with a sample of 278 visually-classified disk galaxies with $M_{\star} > 10^{10} M_{\odot}$ (both centrals and satellites; dashed histogram in the upper-right panel of [Figure 1](#)). As shown in [W.-T. He et al. \(2025\)](#), 30–60% of morphologically disky systems host dominant spheroidal components (e.g., Sombrero galaxy in [D. A. Gadotti & R. Sánchez-Janssen 2012](#)). Such disks, formed by reformation after dry major mergers, are typically embedded in massive stellar halos ([M. Du et al. 2021](#)). Despite exhibiting low kinematically-defined disk mass fractions, they retain observational disk classifications due to features like spiral arms, ongoing star formation, or bars.

2.3. Data extraction and classification of surface density profiles

We derived one-dimensional (1D) surface density profiles from the face-on view using radial annuli with a constant interval of 0.1 kpc. These profiles were fitted with a model consisting of a Sérsic bulge and an exponential disk (see the left panels in [Figure 1](#) for examples), where the initial parameters were estimated from separate fits to the inner and outer regions under visual judgment. This fitting procedure yielded the disk scale length (h_R) and the bulge Sérsic index (n). The outer boundary for the fit is set at the smaller of 30 kpc or the radius where the surface density falls below $10^6 M_{\odot} \text{ kpc}^{-2}$, following [N. Chamba et al. \(2020\)](#) and [I. Trujillo et al. \(2020\)](#). As illustrated in the left panels of [Figure 1](#), we classify such galaxies based on the residuals of this fit in their outer parts: Type I (residuals within ± 0.2 dex), Type II (down-bending, residual < -0.2 dex), and Type III (up-bending, residual > 0.2 dex). The break radius R_{break} , marked by black dashed lines, is defined as the largest radius where the residual is equal to zero.

Five galaxies from the parent sample were excluded due to ambiguous profiles. Our main sample comprises 418 central, disk-dominated galaxies, with subsamples classified as 161 Type I (38.5%), 141 Type II (33.7%), and 116 Type III (27.8%) disk profiles. As illustrated in the right-lower panel of [Figure 1](#) (solid profiles and histograms), these types exhibit distinct stellar mass dependencies. Galaxies with a Type I disk (yellow) account for $\sim 30 - 50\%$ of disk galaxies across a broad mass range ($10^{10} - 10^{11.2} M_{\odot}$). Galaxies with a Type II

disk (blue) account for $\sim 40\%$ of disk galaxies at the low-mass end ($< 10^{10.6} M_{\odot}$) but decline sharply at higher masses ($> 10^{10.6} M_{\odot}$). Conversely, the Type III (pink) fraction dramatically increases from 20% to 60% across the same mass range. We emphasize that our main sample, limited to kinematically-selected central disks, cannot directly benchmark morphology-based observational samples.

For direct comparison with observations, we combine our primary selection with visually-defined disk galaxies (including satellites) to create an augmented sample of 696 galaxies, as illustrated in the right panels of [Figure 1](#) (dashed profiles and histograms). This inclusion of morphologically-selected galaxies does not significantly alter our findings in comparison with the main sample (solid profiles). Crucially, the augmented sample successfully reproduces both the mass-dependent trends and the relative abundances of the dominant profile types found by [Y. Tang et al. \(2020\)](#) (squares), who used SDSS r' -band images of nearly face-on disk galaxies in the redshift range $0.01 < z < 0.15$, with radial coverage extending to $\sim 2.5 R_e$. We also compare our results with those of [J. Laine et al. \(2016\)](#) (triangles), who classified 753 nearly face-on nearby galaxies with Hubble types $-2 < T \leq 9$ and $8.5 \leq \log_{10}(M_{\star}/M_{\odot}) \leq 11$, using $3.6 \mu\text{m}$ images from the S⁴G survey and K_s -band images from the NIRSOS survey. Overall, the Type II and Type III fractions in TNG show broad agreement with observations: at low masses ($< 10^{10.6} M_{\odot}$), Type II disks dominate ($\sim 40\%$ of galaxies), consistent with both [Y. Tang et al. \(2020\)](#) and [J. Laine et al. \(2016\)](#), while Type III fractions show an increasing trend with stellar mass in both simulations and observations. However, [J. Laine et al. \(2016\)](#) found Type II fractions that increase with stellar mass, in contrast to the declining trend seen in both TNG and [Y. Tang et al. \(2020\)](#). Notable discrepancies also remain for the Type I fractions, which are systematically higher in our classification. This may be due to differences in classification criteria adopted across studies. At low masses, the discrepancy appears primarily between the Type I and Type III fractions, whereas at high masses it shifts to the Type I and Type II fractions. Notably, this discrepancy widens when visually classified disk galaxies are included, suggesting that sample selection methods are not the primary driver of these differences. The low Type II fraction in the $10^{10.6} - 10^{11} M_{\odot}$ range may partly arise from the limited volume of TNG-50, which undersamples massive galaxies, the efficient AGN kinetic feedback ([R. Weinberger et al. 2018](#)) that suppresses the young stars essential for prominent breaks, and the un-

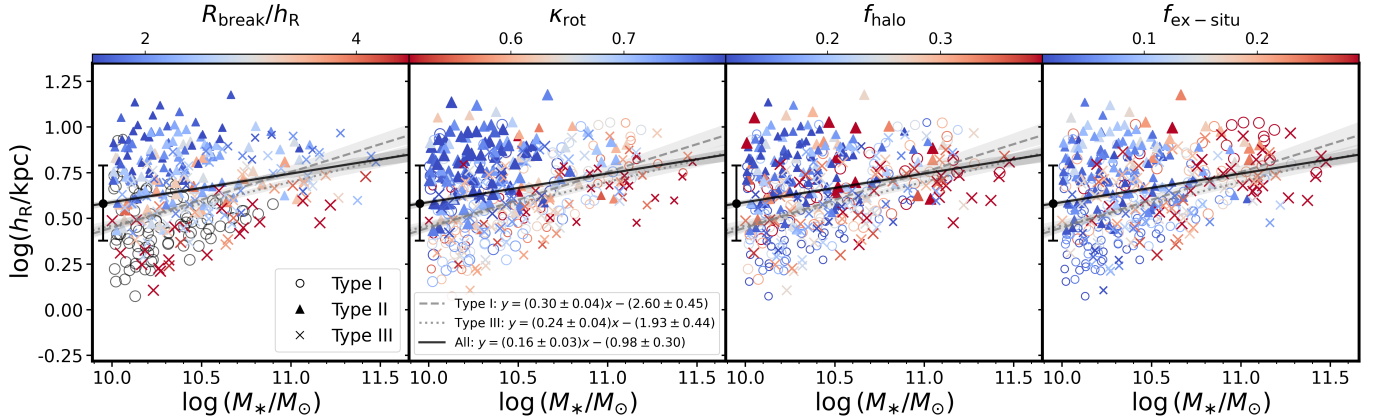


Figure 2. Kinematic and structural properties of Type I (circles), Type II (triangles), and Type III (crosses) galaxies in the h_R – M_* plane. From left to right, the data points are color-coded by the ratio of break radius to inner disk scale length R_{break}/h_R , rotational support κ_{rot} , stellar halo mass fraction f_{halo} , and ex-situ stellar mass fraction $f_{\text{ex-situ}}$. In each panel, the symbol size scales with the corresponding color-coded quantity. The gray dashed, gray dotted, and black solid lines represent the linear fits to the h_R – M_* relation for Type I, Type III, and the total disk sample, respectively; shaded regions denote the 1σ fitting uncertainties. The error bars indicate the standard deviation of the residuals from the global linear fit.

derrepresentation of bar-driven resonance effects (J. C. Muñoz-Mateos et al. 2013; J. Laine et al. 2014).

In the following analysis, we primarily focus on the main sample for simplicity. This study gains insights into the origins of the diverse surface density profiles of disk galaxies.

3. GENERAL PROPERTIES AND MERGER IMPACT OF GALAXIES EXHIBITING DIFFERENT TYPES OF BREAKS

3.1. Difference in galaxy compactness and break radius

Type I (circles) and Type III disks (crosses) exhibit fundamentally distinct scaling relations compared to Type II cases (triangles), as shown in the mass–size diagram (Figure 2). Both Type I and Type III disk galaxies obey a mass–size relation characterized by greater compactness across a broad mass range ($> 10^{10} M_\odot$) – with Type I/III disks dominating the high-mass regime ($\gtrsim 10^{10.6} M_\odot$). In contrast, Type II disks are exclusively confined to lower masses ($\lesssim 10^{10.6} M_\odot$) while showing anomalously large sizes. Linear fitting gives $\log(h_R/\text{kpc}) = (0.30 \pm 0.04) \log(M_*/M_\odot) - (2.60 \pm 0.45)$ for Type I disks (gray dashed lines) and $\log(h_R/\text{kpc}) = (0.24 \pm 0.04) \log(M_*/M_\odot) - (1.93 \pm 0.44)$ for Type III disks (gray dotted lines). The two relations have similar slopes and differ only slightly in $\log h_R$ at fixed stellar mass. For comparison, the fitting result of all disk galaxies is $\log(h_R/\text{kpc}) = (0.16 \pm 0.03) \log(M_*/M_\odot) - (0.98 \pm 0.30)$ (black solid lines). Most of the Type II disk galaxies are above this line. Our findings align with observational results from J. Wang et al. (2018), who analyzed a comparable sample of face-on disk galaxies selected from SDSS r' -band imaging. In lower-mass

galaxies with $\log(M_*/M_\odot) \lesssim 10.6$, they demonstrated that the fraction of cases with a Type II break increases sharply toward lower concentrations ($R_{90}/R_{50} < 2.2$), reaching values near 70%. This correlation indicates that galaxies with Type II breaks possess systematically more extended disks.

As evidenced in the first panel of Figure 2, Type III profiles systematically exhibit larger normalized break radii (R_{break}/h_R) compared to Type II systems. We establish that this distinction stems primarily from differences in scale length h_R rather than absolute break radii R_{break} , which show comparable magnitudes between types. Type II disks display larger h_R (median = 6.39 kpc, mean = 6.55 kpc), resulting in somewhat smaller R_{break}/h_R (median = 2.21, mean = 2.29), while Type III systems possess shorter h_R (median = 4.09 kpc, mean = 4.38 kpc), producing extended normalized breaks (median = 2.74, mean = 3.09). This parameter shows only weak stellar-mass dependence across our sample. Our findings align with M. Pohlen & I. Trujillo (2006)’s SDSS r' -band analysis reporting a smaller mean $R_{\text{break}}/h_R \simeq 2.5$ for Type II versus $\simeq 4.9$ for Type III disks. TNG50 simulations thus plausibly reproduce observed distinctions between down-bending (Type II) and up-bending (Type III) profiles.

3.2. Rotation and potential impact of mergers

Kinematic measurements from Figure 2 (second panel) systematically differentiate the three disk types: Type II disks exhibit the strongest rotational support (median $\kappa_{\text{rot}} = 0.75$), whereas Type III disks show weaker rotational coherence (median $\kappa_{\text{rot}} = 0.63$). Type I systems are kinematically intermediate (median

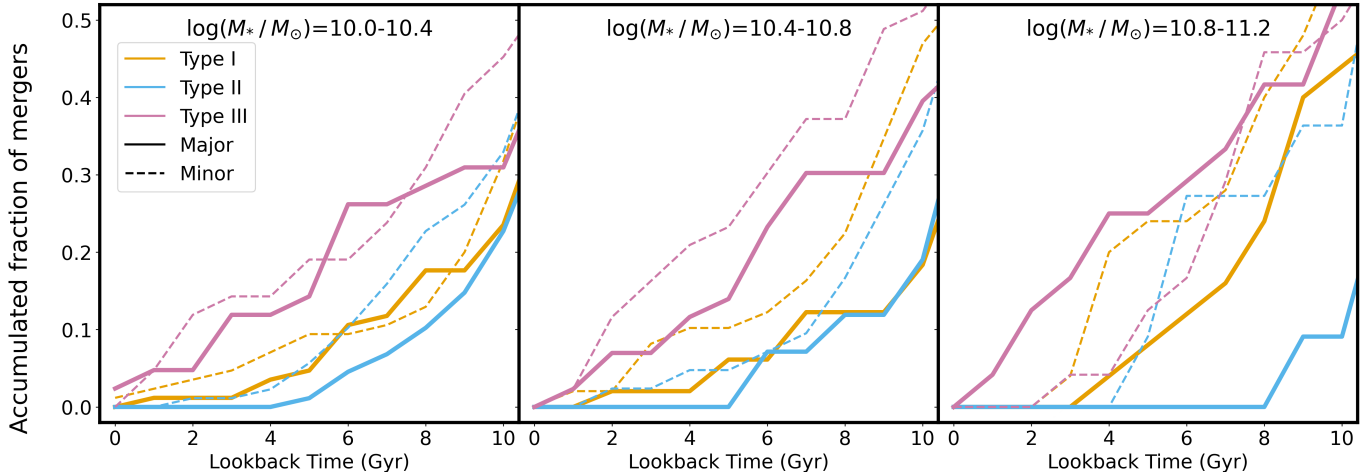


Figure 3. Accumulated fraction of mergers for Type I (yellow), Type II (blue), and Type III (pink) disk galaxies across three stellar mass bins: $\log(M_*/M_\odot) = 10.0\text{--}10.4$ (left), $10.4\text{--}10.8$ (middle), and $10.8\text{--}11.2$ (right). The fraction of galaxies experiencing at least one major merger (solid profiles, mass ratio $> 1 : 4$) or minor merger (dashed profiles, mass ratio $1 : 4\text{--}1 : 10$) as a function of lookback time.

$\kappa_{\text{rot}} = 0.66$). This result qualitatively aligns with [J. Wang et al. \(2018\)](#), who reported Type II disk galaxies as exhibiting markedly higher angular momentum than their Type I and Type III counterparts. A comparable correlation between down-bending profiles and enhanced rotational support is also achieved in the EAGLE simulation, where [J. L. Pfeffer et al. \(2022\)](#) report a steep rise in Type II fraction with increasing κ_{co} , reaching $\gtrsim 80\%$ in the highest- κ_{co} bin for field galaxies.

In the third and fourth panels of [Figure 2](#), the stellar halo mass fractions (f_{halo}) and the ex-situ stellar mass fractions ($f_{\text{ex-situ}}$), both used as merger diagnostics, reveal a consistent ordering in merger activity. In-situ and ex-situ stars are distinguished based on their birth radius in spherical coordinates ($r_{\text{birth,3D}}$): in-situ stars are those formed with $r_{\text{birth,3D}} \leq 30$ kpc, while ex-situ stars are those with $r_{\text{birth,3D}} > 30$ kpc. We derive stellar birth coordinates by transforming native TNG simulation formation positions into galaxy rest frames using [GalaxyPose \(S. Lu 2026\)](#). Each frame is reconstructed per snapshot using the central position, bulk stellar velocity, and angular momentum vector evolution of progenitor galaxies. Orbital trajectories and orientation functions achieve temporal continuity through cubic spline interpolation and spherical linear interpolation (slerp), respectively. The resulting positional uncertainty is less than 1 kpc, which is negligible for both the radial density profile analysis and computation of global galaxy parameters performed here.

Type II disks have the weakest merger signatures (median $f_{\text{halo}} = 0.14$, $f_{\text{ex-situ}} = 0.05$), Type III the strongest (median $f_{\text{halo}} = 0.26$, $f_{\text{ex-situ}} = 0.19$), and Type I systems lie in between (median $f_{\text{halo}} = 0.20$, $f_{\text{ex-situ}} =$

0.08). [T. Ruiz-Lara et al. \(2017\)](#) obtained a similar conclusion using Milky Way analogues in the RaDES cosmological simulations. [Figure 3](#) traces the cumulative merger histories for the three galaxy types across three stellar mass bins: $\log(M_*/M_\odot) = 10.0\text{--}10.4$ (low), $10.4\text{--}10.8$ (intermediate), and $10.8\text{--}11.2$ (high). We define the merger mass ratio μ as $\mu \equiv M_{\star,\text{sec}}^{\text{max}}/M_{\star,\text{pri}}$, where $M_{\star,\text{sec}}^{\text{max}}$ is the maximum historical stellar mass attained by the secondary progenitor, and $M_{\star,\text{pri}}$ is the primary’s stellar mass at the final snapshot where SUBFIND ([V. Springel et al. 2001](#)) identifies the secondary as an independent subhalo. Type II (blue) galaxies exhibit the lowest merger frequencies for both major ($\mu > 0.25$; solid) and minor mergers ($0.1 \leq \mu \leq 0.25$; dashed). Conversely, Type III (pink) systems show the highest major merger fractions across all masses, increasing with stellar mass, while their minor-merger fractions peak at low-to-intermediate masses. Type I (yellow) displays intermediate major merger frequencies but dominates in minor mergers at high masses, suggesting Types I and III result from distinct external perturbation regimes.

These results indicate Type II break galaxies evolve predominantly through internal (“secular”) processes, i.e., the natural evolutionary pathway, retaining high rotational velocities and large disk sizes due to minimal merger/tidal disruption. Consequently, they exhibit stronger rotational support and less massive stellar halos than Type I/III systems. In contrast, Type III (up-bending) breaks originate primarily from merger events that supply accreted stars while disrupting outer disk structure ([K. Bekki 1998](#); [J. Aguerri et al. 2001](#); [M. C. Eliche-Moral et al. 2006](#)). Both major and minor mergers ([A. Borlaff et al. 2014](#)) likely contribute to Type I/III

break formation. Type II systems thus serve as optimal laboratories for probing merger-free secular evolution and constitute primary targets for studying undisturbed assembly histories. Detailed analysis of Type III disk galaxies is beyond the scope of this paper.

4. ORIGIN OF TYPE II DISKS AND THEIR U-SHAPED AGE PROFILES

The formation of Type II disk breaks is primarily interpreted through two physical channels: radial migration and star formation truncation. The first involves the outward redistribution of stars driven by non-axisymmetric features (V. P. Debattista et al. 2006; J. Herpich et al. 2017), which can explain observed U-shaped stellar age profiles (Z. Zheng et al. 2015; D. A. Dale et al. 2015). Alternatively, the second channel attributes the breaks to an abrupt radial change in star formation profiles (J. L. Pfeffer et al. 2022; Y. Tang et al. 2020). However, as star formation ceases beyond the break radius in this scenario, it cannot naturally account for the presence of old stellar populations at large radii. To reconcile this, these models typically invoke outward radial migration to transport old stars into the outer disk (R. Roškar et al. 2008; Y. Tang et al. 2020) or an extended stellar halo contribution (J. L. Pfeffer et al. 2022); without these contributions, star-formation-driven models struggle to explain the stellar distribution beyond the break. In the following analysis, we investigate what mechanism primarily drives the formation of Type II profiles in TNG50.

The TNG simulations reasonably model gas cycles and star formation physics at low redshifts ($z \leq 1$), as evidenced by their consistency with SDSS observations of the galaxy stellar mass function (GSMF) and color bimodality (D. Nelson et al. 2018b), and significantly improved agreement with HI data relative to its predecessor Illustris (H. Guo et al. 2020). This robust validation establishes TNG as a credible theoretical framework for studying structural evolution and formation mechanisms of Type II disk galaxies.

4.1. A New Channel Driven by Inside-out Growth of Cold Gas Accretion and sSFR

To reveal the physical drivers behind the formation of Type II disks, we trace the evolution of their radial profiles from $z = 1.5$ to $z = 0$ (Figure 4). The solid profiles show the median values for Type II disk galaxies as a function of normalized radius (R/R_{break}), where each galaxy profile was first computed in 0.3 kpc annuli and then mapped to normalized radius using R_{break} ($z = 0$). For consistency, $\Sigma_{\text{cold gas}}$ is computed using gas cells selected to lie close to the disk mid-plane ($|z| \leq 3$ kpc)

and to have $\text{SFR} > 0$ within a cylindrical radius of $R \leq 30$ kpc; the same selection is applied when computing Σ_{SFR} (and hence sSFR and SFE). The stellar age profile calculation includes all stars within a cylindrical radius of $R \leq 30$ kpc. We find that the profiles exhibit synchronized evolutionary features. At $z \geq 1$ (blue and gray), the normalized galaxy density profiles generally have no down-bending break and the age profiles are quite flat, as shown in the first and second panels of Figure 4, with no U-shape present. As the system evolves to $z \sim 0.5$ (pink), a Type II break in the normalized density profile gradually emerges, closely accompanied by the formation of a U-shaped age profile. This feature persists and strengthens until $z = 0$ (yellow). A flattened U-shaped age profile in older stellar populations is also found in TNG Type II galaxies, consistent with the findings of D. J. Radburn-Smith et al. (2012) (see Appendix A for details).

This structural transformation coincides closely with the evolution of the cold-gas distribution and the specific star formation rate (sSFR), as shown in the third and fourth panels of Figure 4. The stellar surface-density profile at $z \sim 1$ remains nearly single-exponential beyond the present-day break radius; consequently, the secular flattening of $\Sigma_{\text{cold, gas}}$ since $z \leq 0.5$ (pink and yellow) induces a localized enhancement of sSFR around R_{break} , thereby producing a radial break. This localized enhancement drives increased stellar mass assembly at R_{break} relative to both the interior and exterior disk regions, resulting in a down-bending exponential profile. A similar connection between R_{break} and the gas/star-formation rate (SFR) profile truncation was also noted by R. Roškar et al. (2008), aligning with our findings in TNG50. Importantly, the bottom panel of Figure 4 confirms that the star formation efficiency (SFE) profiles remain spatially flat and temporally constant. This demonstrates that the radial break does not originate from localized variations in star formation physics, but is a structural consequence of the sSFR peak. Moreover, the truncation radius of the cold gas surface density ($\Sigma_{\text{cold gas}}$), the peak position of the sSFR, as well as R_{break} and the minimum of the U-shaped age profile, are consistent and all shift outward with time. This effectively explains the phenomenon that the radial position of the break has been found to increase with cosmic time (I. Trujillo & M. Pohlen 2005; R. Azzollini et al. 2008).

While P. Sánchez-Blázquez et al. (2009) similarly observed a Type II break in the cosmological hydrodynamical simulation of a single disk galaxy, these features manifested exclusively in young stellar populations, with no discernible break in the total surface density profile. They attributed the U-shaped age profiles primarily to

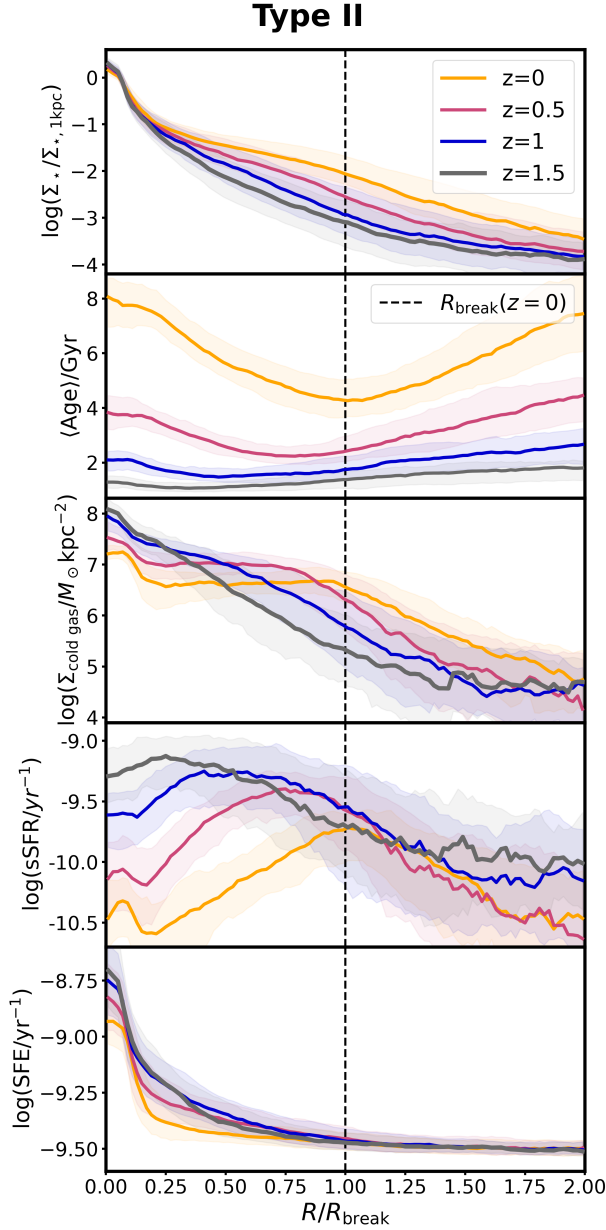


Figure 4. Evolution of radial profiles for Type II disk galaxies from $z = 1.5$ to $z = 0$, plotted against the normalized radius R/R_{break} . The panels represent, from top to bottom: normalized stellar surface density ($\Sigma_*/\Sigma_{*,1\text{kpc}}$), mass-weighted mean stellar age computed from all stellar particles within a cylindrical radius of $R \leq 30$ kpc, cold gas surface density ($\Sigma_{\text{cold gas}}$), specific star formation rate (sSFR), and star formation efficiency (SFE). Colored curves correspond to different redshifts: $z = 0$ (yellow), $z = 0.5$ (pink), $z = 1.0$ (blue), and $z = 1.5$ (gray). Solid lines denote the median values, while shaded regions indicate the interquartile range (25th–75th percentiles). The vertical dashed line marks the break radius identified at $z = 0$.

the sharp SFR decline beyond the break radius—a mechanism related to but distinct from our results, as their

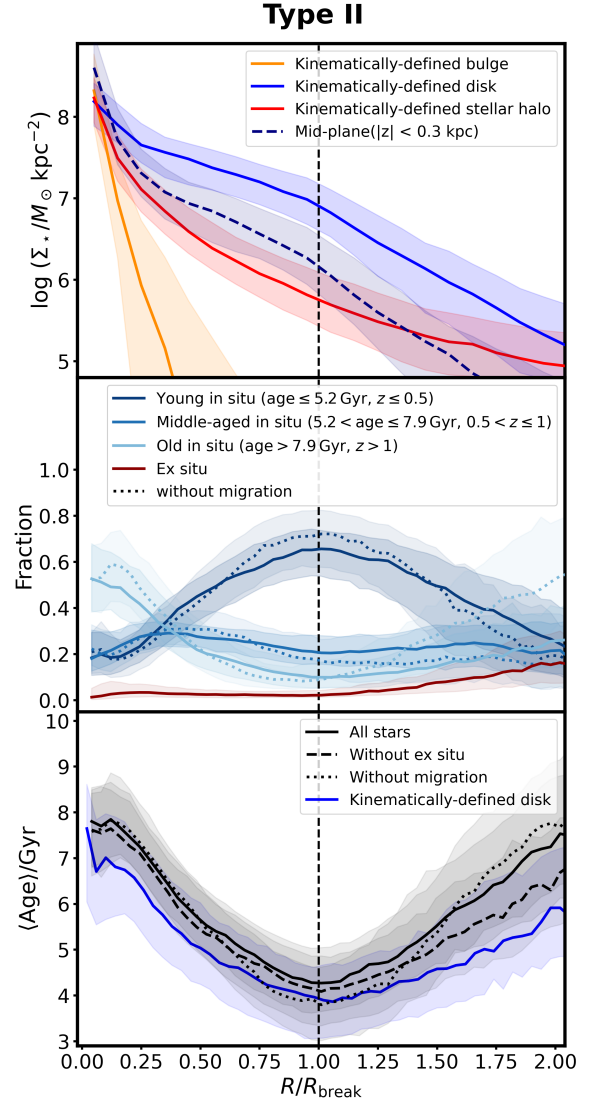


Figure 5. **Top panel:** radial surface density profiles for the kinematically-defined disk (blue), bulge (yellow), and stellar halo (red), following the decomposition method of M. Du et al. (2019, 2020), along with the surface density profile of mid-plane stars ($|z| < 0.3$ kpc, dark blue dashed). **Middle panel:** radial mass fractions of ex-situ stars (brown) and in-situ stars. The in-situ population is subdivided into three age bins: young, intermediate-age, and old (dark to light blue shading). Dotted lines represent the distributions excluding radial migration. **Bottom panel:** radial mass-weighted age profiles for all stellar particles within a cylindrical radius of $R \leq 30$ kpc (black) and the corresponding distributions after excluding ex-situ stars and radial migration, along with the age profile of the kinematically-defined disk component (blue). In each panel, solid lines denote median values, shaded regions indicate the interquartile range (25th–75th percentiles), and the vertical dashed line marks the break radius R_{break} .

sharp decline in SFR happened in warps. Moreover, we

identify localized sSFR enhancement as the direct driver simultaneously producing both Type II breaks and U-shaped age profiles. Since sSFR quantifies the relative formation rate of young stars across radii, it provides the fundamental link between star formation dynamics and structural evolution. Furthermore, we visually verified that inside-out growth of sSFR peaks has no clear link with the appearance of warps.

The Type II break constitutes a fundamental structural signature of dynamical cold disks themselves, rather than a feature that merely reflects the relative importance of the disk compared to the spheroid. By utilizing the kinematic decomposition from *M. Du et al. (2019, 2020)*, the top panel of Figure 5 shows clearly that the outer regions (extending to $2 \times R_{\text{break}}$) are dominated by rotationally supported disk components. The break radius identified in the kinematic disk density profile aligns with that of the total surface density profile. We further verified that mid-plane stars ($|z| < 0.3 \text{ kpc}$) of Type II disk galaxies exhibit a prominent down-bending break in their surface density profile (dark-blue profile in the top panel); furthermore, the cold kinematics of the outer disk confirm that the age upturn beyond R_{break} is free from spheroidal contamination (see Appendix B for details). These results suggest that the formation of Type II breaks is largely dominated by rotationally supported structures rather than spheroidal components (e.g., the stellar halo). For Type II disk galaxies in their comparable mass range ($\log(M_*/M_\odot) \sim 10\text{--}11$), stellar halos show systematically lower surface densities of ~ 1 dex than their disk counterparts, despite minor differences in total stellar mass among galaxies (which we neglect). Such stellar halos thus exhibit negligible contributions beyond R_{break} and cannot reproduce the outer-disk part of the observed U-shaped age profiles.

Type II profile formation aligns closely with the “extended galaxies” evolutionary track identified in *H.-C. Ma et al. (2024)*. The emergence of Type II features at $z \sim 0.5$ stems from delayed angular momentum (j) transfer: dark matter halo \rightarrow total gas \rightarrow cold gas. This process yields a few Gyr lag between the specific angular momentum evolution of cold gas ($j_{\text{cold gas}}$, shown in their Figure 6) and total gas (j_{gas}). The delay implies that cosmic environment-driven j -gains require finite time to restructure cold gas distributions and stellar disks. Physically, late-phase accretion ($z < 1$) injects high- j gas that settles preferentially at outer regions of disks rather than their centers, directly driving the inside-out growth of cold gas density and Type II breaks.

4.2. Demographics of Stars of Down-bending Breaks: In-situ Formation, Radial Migration, and Ex-situ Accretion

Building on evidence from the preceding section that Type II breaks form gradually at $z < 1$, we isolate potential contributions from alternative mechanisms by decomposing $z = 0$ stellar populations by origin (in situ vs. ex situ) and formation time. Further, we divide in-situ stars into three age cohorts shown in Figure 5 (middle panel, from dark to light blue): young (age ≤ 5.2 Gyr, $z \leq 0.5$), middle-aged ($5.2 \text{ Gyr} < \text{age} \leq 7.9 \text{ Gyr}$, $0.5 < z \leq 1$), and old (age > 7.9 Gyr, $z > 1$). Note that this decomposition includes all stars in the galaxy rather than being restricted to kinematically-defined disk components. In Type II systems, young in-situ stars dominate the stellar mass budget around R_{break} , contributing $\sim 70\%$ of the total, while ex-situ stars remain negligible ($< 10\%$, brown profile) across a broad radial range, extending out to $\sim 1.7 R_{\text{break}}$, and thus cannot explain U-shaped age profiles. To isolate radial redistribution effects, we compute the birth-radius-dependent fraction of young stars (dark-blue dotted lines) using the cylindrical birth radius ($R_{\text{birth,2D}}$), representing a no-migration scenario. Although older stars migrate over longer timescales, the comparison between profiles with and without migration (solid vs. dotted lines) shows that they diffuse throughout the disk rather than accumulating in the outskirts, leading to a decreased relative fraction in the outer disk. As demonstrated in the bottom panel of Figure 5, the age profile of the kinematically defined disk component exhibits a clear U-shaped profile (blue line), confirming that the age upturn is not an artifact of spheroidal contamination. Our comparative analysis further shows that removing ex-situ stars has a minimal effect on the age gradient (black-dashed line), while excluding the migration effect actually yields a stronger and steeper U-shaped upturn (black dotted line). These findings confirm that radial migration is not the cause of the U-shape; instead, it acts to weaken both the break (*P. Sánchez-Blázquez et al. 2009; Y. Tang et al. 2020*) and the age upturn by diluting the localized stellar assembly at R_{break} .

For quantitative analysis, measurements for Type II disk galaxies reveal the origins of stars in the outer disk ($R > R_{\text{break}}$). To account for orbital eccentricity of stars, migrated stars are specifically defined as those with $R_{\text{birth,2D}} < R_{\text{break}} - 2 \text{ kpc}$. Based on this criterion, median contributions to the outer disk comprise 60% in-situ formation, 33% migrated in-situ stars from inner regions, and 5% ex-situ stars from early mergers, all of which are calculated using stars across all age bins.

S. Lu et al. (2025) showed that in TNG simulations, both bar fractions and lengths are smaller than observed galaxies with $M_\star < 10^{10.5} M_\odot$ — the mass regime where Type II disks prevail. Although this may reduce radial migration efficiency, we emphasize that 45% of Type II disks remain unbarred. The high prevalence of Type II breaks in unbarred galaxies suggests that bars play a subordinate role in Type II break formation.

Beyond the local Universe, we also compare our classification with high-redshift observations from D. Xu & S.-Y. Yu (2024); S.-Y. Yu et al. (2025), who classified 247 nearly face-on disk galaxies with $\log(M_\star/M_\odot) > 10$ at $1 \leq z \leq 3$ using JWST/CEERS F356W images. For a comparable sample of 247 disk galaxies at $z = 1$ in TNG-50, we find Type I: 36.1%, Type II: 9.5%, and Type III: 54.4%, whereas D. Xu & S.-Y. Yu (2024) reported Type I: 12.6%, Type II: 56.7%, and Type III: 34.8%. The substantially lower Type II fraction lies beyond this study’s scope, given the challenges in both simulating and observing high-redshift galaxies. Moreover, the U-shaped age profile is not prominent in high-redshift Type II galaxies, consistent with the observations of S.-Y. Yu et al. (2025). At high redshift, galaxies are too young to have developed a pronounced age contrast between the inner and outer disc, such that the amplitude of the U-shaped signal may not yet have reached a level that can be clearly identified, consistent with both high-redshift observations (e.g., S.-Y. Yu et al. 2025) and TNG simulations. The radial profile evolution of high-redshift Type II galaxies is considerably more complex, and a detailed investigation of the underlying mechanisms is beyond the scope of this paper. We note that inside-out growth is the primary formation mechanism for Type II breaks in our sample, while the influence of other mechanisms cannot be ruled out, particularly at high redshift where observational uncertainties remain large.

5. SUMMARY

Our analysis of 418 central disk galaxies ($M_\star > 10^{10} M_\odot$) from the TNG50 simulation demonstrates that simulated galaxies reproduce key observed trends: mass-dependent abundances, structural scaling relations, and the morphological segregation where Type II disks dominate low-mass systems ($\sim 40\%$) with unusually large sizes, while Type III becomes prevalent at high masses ($> 10^{10.6} M_\odot$) with greater compactness.

Systematic diagnostics reveal fundamental differences in disk types: Type II systems show signatures of dynamically cold, undisturbed disks – maximal rotational support, minimal spheroidal and ex-situ components (median $\sim 14\%$ and $\sim 5\%$ respectively), and quies-

cent merger histories. Type III systems exhibit the opposite characteristics: weakest rotational coherence, highest spheroidal and ex-situ fractions (median $\sim 26\%$ and $\sim 19\%$ respectively), and merger-driven evolution. Type I consistently occupies intermediate parameter space. This supports a framework where Type II profiles represent the intrinsic disk state in isolation, with Type I and Type III emerging from progressively stronger external perturbations – moderate and major disturbances, respectively.

A new scenario is proposed that the inside-out growth of cold-gas accretion and star formation causes Type-II breaks and their associated U-shaped age profiles. Tracking these features from $z = 1.5$ to $z = 0$ reveals a critical transition around $z \sim 0.5$, when both properties develop concurrently with: (1) long-term flattening of the cold gas density profiles, and (2) a localized sSFR peak around the break radius. This concentrated starburst accelerates stellar mass assembly, preferentially flattening the inner surface density profile relative to the outer disk. Such a break gradually expands to larger regions. Beyond the Type-II break radius, $\sim 33\%$ of stars originate from radial migration of stars born at inner regions, and only $\sim 5\%$ of stars are accreted from ex-situ origin. Galaxies with a Type II break are thus likely to be ideal cases for studying the evolution of galaxies in nature where both mergers and environmental effects are minimal.

ACKNOWLEDGMENTS

We are grateful to the referee for the insightful and constructive report, which has substantially improved the quality and clarity of the letter. This work is supported by the National Key R&D Program of China (No. XY-2025-1459), the National Natural Science Foundation of China under grant No. 12573010, and the Science Fund for Creative Research Groups of the National Natural Science Foundation of China (No. 12221003). J.L. would like to acknowledge the NSFC under grant 12273027. LCH is supported by the National Science Foundation of China (12233001) and the China Manned Space Program (CMS-CSST-2025-A09). The TNG50 simulation used in this work, one of the flagship runs of the IllustrisTNG project, has been run on the HazelHen Cray XC40-system at the High Performance Computing Center Stuttgart as part of project GCS-ILLU of the Gauss Centers for Supercomputing (GCS). This work is also strongly supported by the Computing Center in Xi’an, China.

REFERENCES

- Abadi, M. G., Navarro, J. F., Steinmetz, M., & Eke, V. R. 2003, *The Astrophysical Journal*, 597, 21
- Aguerri, J., Balcells, M., & Peletier, R. 2001, *Astronomy & Astrophysics*, 367, 428
- Azzollini, R., Trujillo, I., & Beckman, J. E. 2008, *The Astrophysical Journal*, 684, 1026
- Bekki, K. 1998, *The Astrophysical Journal*, 502, L133
- Borlaff, A., Eliche-Moral, M. C., Rodríguez-Pérez, C., et al. 2014, *Astronomy & Astrophysics*, 570, A103
- Brunetti, M., Chiappini, C., & Pfenniger, D. 2011, *Astronomy & Astrophysics*, 534, A75
- Chamba, N., Trujillo, I., & Knapen, J. H. 2020, *Astronomy & Astrophysics*, 633, L3
- Cooper, A. P., D'Souza, R., Kauffmann, G., et al. 2013, *Monthly Notices of the Royal Astronomical Society*, 434, 3348
- Dale, D. A., Beltz-Mohrmann, G. D., Egan, A. A., et al. 2015, *The Astronomical Journal*, 151, 4
- Davis, M., Efstathiou, G., Frenk, C. S., & White, S. D. 1985, *Astrophysical Journal*, Part 1 (ISSN 0004-637X), vol. 292, May 15, 1985, p. 371-394. Research supported by the Science and Engineering Research Council of England and NASA., 292, 371
- De Jong, R. S., Seth, A., Radburn-Smith, D., et al. 2007, *The Astrophysical Journal*, 667, L49
- Debattista, V. P., Mayer, L., Carollo, C. M., et al. 2006, *The Astrophysical Journal*, 645, 209
- Díaz-García, S., Salo, H., & Laurikainen, E. 2016, *Astronomy & Astrophysics*, 596, A84
- Doménech-Moral, M., Martínez-Serrano, F., Domínguez-Tenreiro, R., & Serna, A. 2012, *Monthly Notices of the Royal Astronomical Society*, 421, 2510
- Du, M., Ho, L. C., Debattista, V. P., et al. 2021, *The Astrophysical Journal*, 919, 135
- Du, M., Ho, L. C., Debattista, V. P., et al. 2020, *The Astrophysical Journal*, 895, 139
- Du, M., Ho, L. C., Zhao, D., et al. 2019, *The Astrophysical Journal*, 884, 129
- Dutton, A. A., & Van Den Bosch, F. C. 2009, *Monthly Notices of the Royal Astronomical Society*, 396, 141
- Eliche-Moral, M. C., Balcells, M., Prieto, M., et al. 2006, *The Astrophysical Journal*, 639, 644
- Erwin, P., Beckman, J. E., & Pohlen, M. 2005, *The Astrophysical Journal*, 626, L81
- Erwin, P., Gutiérrez, L., & Beckman, J. E. 2012, *ApJL*, 744, L11, doi: [10.1088/2041-8205/744/1/L11](https://doi.org/10.1088/2041-8205/744/1/L11)
- Freeman, K. C. 1970, *Astrophysical Journal*, vol. 160, p. 811, 160, 811
- Gadotti, D. A., & Sánchez-Janssen, R. 2012, *Monthly Notices of the Royal Astronomical Society*, 423, 877
- Guo, H., Jones, M. G., Haynes, M. P., & Fu, J. 2020, *The Astrophysical Journal*, 894, 92
- Gutiérrez, L., Erwin, P., Aladro, R., & Beckman, J. E. 2011, *The Astronomical Journal*, 142, 145
- He, W.-T., Du, M., Li, Z.-Y., & Li, Y. 2025, *Astronomy & Astrophysics*, 699, A99
- Herpich, J., Stinson, G. S., Rix, H.-W., Martig, M., & Dutton, A. A. 2017, *Monthly Notices of the Royal Astronomical Society*, 470, 4941
- Laine, J., Laurikainen, E., & Salo, H. 2016, *Astronomy & Astrophysics*, 596, A25
- Laine, J., Laurikainen, E., Salo, H., et al. 2014, *Monthly Notices of the Royal Astronomical Society*, 441, 1992
- Lian, J., Wang, T., Feng, Q., Huang, Y., & Guo, H. 2025, *The Astrophysical Journal Letters*, 990, L37
- Lian, J., Zasowski, G., Chen, B., et al. 2024, *Nature Astronomy* doi, 10
- Lu, S. 2026, *GalaxyPose*, Zenodo, doi: [10.5281/zenodo.18212505](https://doi.org/10.5281/zenodo.18212505)
- Lu, S., Du, M., & Debattista, V. P. 2025, *Astronomy & Astrophysics*, 697, A236
- Ma, H.-C., Du, M., Ho, L. C., Sheng, M.-J., & Liao, S. 2024, *Astronomy & Astrophysics*, 689, A293
- Marinacci, F., Vogelsberger, M., Pakmor, R., et al. 2018, *Monthly Notices of the Royal Astronomical Society*, 480, 5113
- Mo, H., Mao, S., & White, S. D. 1998, *Monthly Notices of the Royal Astronomical Society*, 295, 319
- Mondelin, M., Bournaud, F., Cuillandre, J.-C., & Hennebelle, P. 2025a, *A&A*, 701, A268, doi: [10.1051/0004-6361/202554840](https://doi.org/10.1051/0004-6361/202554840)
- Mondelin, M., Bournaud, F., Cuillandre, J.-C., et al. 2025b, *A&A*, 699, A214, doi: [10.1051/0004-6361/202554838](https://doi.org/10.1051/0004-6361/202554838)
- Muñoz-Mateos, J. C., Sheth, K., Gil de Paz, A., et al. 2013, *ApJ*, 771, 59, doi: [10.1088/0004-637X/771/1/59](https://doi.org/10.1088/0004-637X/771/1/59)
- Naiman, J. P., Pillepich, A., Springel, V., et al. 2018, *Monthly Notices of the Royal Astronomical Society*, 477, 1206
- Nelson, D., Kauffmann, G., Pillepich, A., et al. 2018a, *Monthly Notices of the Royal Astronomical Society*, 477, 450
- Nelson, D., Pillepich, A., Springel, V., et al. 2018b, *Monthly Notices of the Royal Astronomical Society*, 475, 624
- Nelson, D., Springel, V., Pillepich, A., et al. 2019a, *Computational Astrophysics and Cosmology*, 6, 2
- Nelson, D., Springel, V., Pillepich, A., et al. 2019b, *Computational Astrophysics and Cosmology*, 6, 1

- Peng, C. Y., Ho, L. C., Impey, C. D., & Rix, H.-W. 2010, *The Astronomical Journal*, 139, 2097
- Pfeffer, J. L., Bekki, K., Forbes, D. A., Couch, W. J., & Koribalski, B. S. 2022, *Monthly Notices of the Royal Astronomical Society*, 509, 261
- Pillepich, A., Springel, V., Nelson, D., et al. 2018, *Monthly Notices of the Royal Astronomical Society*, 473, 4077
- Pillepich, A., Nelson, D., Springel, V., et al. 2019, *Monthly Notices of the Royal Astronomical Society*, 490, 3196
- Planck Collaboration, Ade, P. A. R., Aghanim, N., et al. 2016, *A&A*, 594, A13, doi: [10.1051/0004-6361/201525830](https://doi.org/10.1051/0004-6361/201525830)
- Pohlen, M., & Trujillo, I. 2006, *A&A*, 454, 759, doi: [10.1051/0004-6361:20064883](https://doi.org/10.1051/0004-6361:20064883)
- Radburn-Smith, D. J., Roškar, R., Debattista, V. P., et al. 2012, *The Astrophysical Journal*, 753, 138
- Roškar, R., Debattista, V. P., Stinson, G. S., et al. 2008, *ApJL*, 675, L65, doi: [10.1086/586734](https://doi.org/10.1086/586734)
- Ruiz-Lara, T., Few, C., Florido, E., et al. 2017, *Astronomy & Astrophysics*, 608, A126
- Ruiz-Lara, T., Pérez, I., Florido, E., et al. 2015, *Monthly Notices of the Royal Astronomical Society: Letters*, 456, L35
- Sales, L. V., Navarro, J. F., Schaye, J., et al. 2010, *Monthly Notices of the Royal Astronomical Society*, 409, 1541
- Sánchez-Alarcón, P., Román, J., Knapen, J., et al. 2023, *Astronomy & Astrophysics*, 677, A117
- Sánchez-Blázquez, P., Courty, S., Gibson, B., & Brook, C. 2009, *Monthly Notices of the Royal Astronomical Society*, 398, 591
- Springel, V. 2010, *Monthly Notices of the Royal Astronomical Society*, 401, 791
- Springel, V., White, S. D., Tormen, G., & Kauffmann, G. 2001, *Monthly Notices of the Royal Astronomical Society*, 328, 726
- Springel, V., Pakmor, R., Pillepich, A., et al. 2018, *Monthly Notices of the Royal Astronomical Society*, 475, 676
- Tang, Y., Chen, Q., Zhang, H.-X., et al. 2020, *The Astrophysical Journal*, 897, 79
- Trujillo, I., Chamba, N., & Knapen, J. H. 2020, *Monthly Notices of the Royal Astronomical Society*, 493, 87
- Trujillo, I., & Pohlen, M. 2005, *The Astrophysical Journal*, 630, L17
- Van Den Bosch, F. C. 2001, *Monthly Notices of the Royal Astronomical Society*, 327, 1334
- Wang, E., & Lilly, S. J. 2022, *The Astrophysical Journal*, 927, 217
- Wang, H.-F., Liu, C., Xu, Y., Wan, J.-C., & Deng, L. 2018, *MNRAS*, 478, 3367, doi: [10.1093/mnras/sty1058](https://doi.org/10.1093/mnras/sty1058)
- Wang, J., Zheng, Z., D'Souza, R., et al. 2018, *Monthly Notices of the Royal Astronomical Society*, 479, 4292
- Weinberger, R., Springel, V., Hernquist, L., et al. 2017, *MNRAS*, 465, 3291, doi: [10.1093/mnras/stw2944](https://doi.org/10.1093/mnras/stw2944)
- Weinberger, R., Springel, V., Pakmor, R., et al. 2018, *Monthly Notices of the Royal Astronomical Society*, 479, 4056
- Xu, D., & Yu, S.-Y. 2024, *Astronomy & Astrophysics*, 682, L17
- Younger, J. D., Cox, T., Seth, A. C., & Hernquist, L. 2007, *The Astrophysical Journal*, 670, 269
- Yu, S.-Y., Xu, D., Kalita, B. S., et al. 2025, *Astronomy & Astrophysics*, 693, L9
- Zheng, Z., Thilker, D. A., Heckman, T. M., et al. 2015, *The Astrophysical Journal*, 800, 120
- Zhong, W., Du, M., Lu, S., Jin, Y., & Zhu, K. 2026, arXiv preprint [arXiv:2602.01098](https://arxiv.org/abs/2602.01098)

APPENDIX

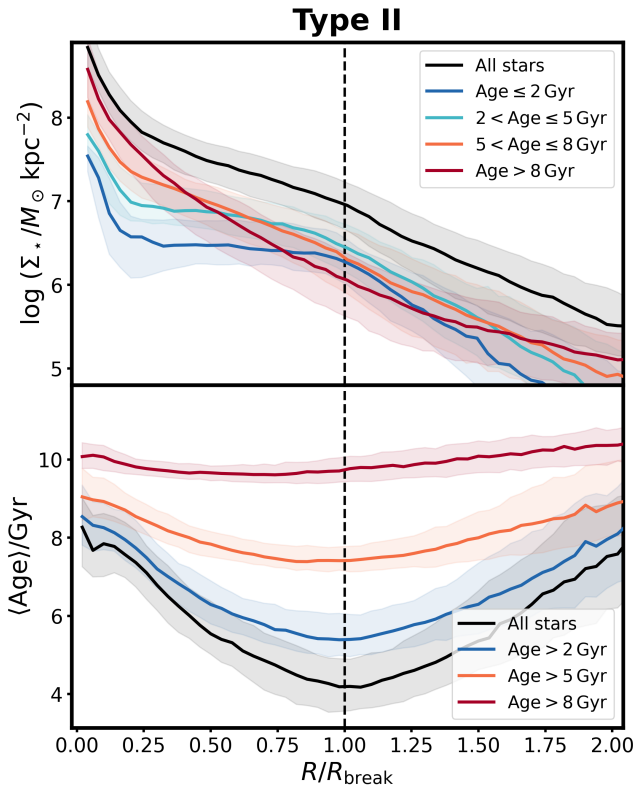


Figure 6. **Upper panel:** Median stellar surface density profiles of Type II disk galaxies for different stellar age populations: all stars, ≤ 2 Gyr, 2–5 Gyr, 5–8 Gyr, and > 8 Gyr. **Lower panel:** Mass-weighted age profiles for progressively older stellar populations: all stars, > 2 Gyr, > 5 Gyr, and > 8 Gyr.

This appendix presents two supplementary analyses in support of the mechanism proposed in this work: Appendix A validates well-known characteristic features of Type II breaks, and Appendix B confirms the cold disc kinematics of Type II disks.

A. PROPERTIES OF TYPE II DISK GALAXIES

We divide the stellar population into four age bins: ≤ 2 Gyr, 2–5 Gyr, 5–8 Gyr, and > 8 Gyr. The upper panel of Figure 6 shows the surface density profiles for each age bin. The youngest population (dark blue) exhibits the sharpest down-bending break, while the break weakens progressively with increasing stellar age. The oldest population (brown) shows a significantly flattened profile with no discernible break, consistent with the findings of *D. J. Radburn-Smith et al. (2012)*. This is a direct consequence of the inside-out growth mechanism proposed in this work: the strongest break appears in the youngest population where the sSFR peaks. The

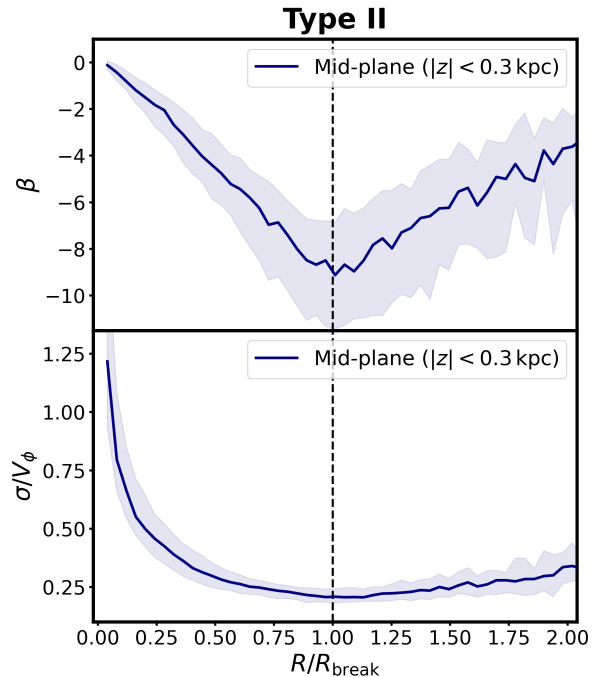


Figure 7. Kinematic diagnostics of Type II disk galaxies. **Upper panel:** velocity anisotropy parameter β as a function of normalized radius R/R_{break} , computed from mid-plane stars ($|z| < 0.3$ kpc). **Lower panel:** ratio of velocity dispersion to mean rotational velocity σ/v_ϕ , computed from mid-plane stars ($|z| < 0.3$ kpc).

lower panel of Figure 6 shows the mass-weighted age profiles. The age profiles become increasingly flat with stellar age, and the oldest population (brown) exhibits an essentially flat radial age distribution. Consistent with inside-out growth of sSFR, Type II breaks primarily trace younger stellar populations. This naturally explains their enhanced prominence in bluer photometric bands, where young stars dominate emission.

B. KINEMATIC PROPERTIES OF TYPE II DISK GALAXIES

To verify that the outer disk beyond R_{break} is kinematically cold and free from significant spheroidal contamination, we present kinematic diagnostics for Type II disk galaxies in Figure 7, computed from all stellar particles within the mid-plane region ($|z| < 0.3$ kpc). In the upper panel, the velocity anisotropy parameter $\beta = 1 - (v_\theta^2 + v_\phi^2)/(2v_r^2)$, where v_r , v_θ , and v_ϕ are the velocity components in polar coordinates, remains consistently negative across the entire radial range, indicating that stellar orbits are dominated by tangential motion. This holds even beyond R_{break} , ruling out signifi-

cant contamination from spheroidal or halo components whose orbits are radially biased. The inflection point of β coincides with R_{break} , reflecting the concentration of dynamically cold young stars at this location, consistent with our conclusions. In the lower panel, the ratio σ/v_ϕ , where $\sigma = \sqrt{(\sigma_R^2 + \sigma_\phi^2 + \sigma_z^2)/3}$ is the root-mean-square velocity dispersion of the three cylindrical components (radial, azimuthal, and vertical), and v_ϕ is the average cylindrical rotational velocity within each radial bin, decreases from ~ 1.25 at the center to ~ 0.25 by $0.5 R_{\text{break}}$ and remains at this low level out to $\sim 1.5 R_{\text{break}}$ with only a marginal increase. This confirms that ordered rotation overwhelmingly dominates over random motion throughout the disk, including beyond R_{break} .